

Surface Cyclolysis in the North Pacific Ocean. Part II: Piecewise Potential Vorticity Diagnosis of a Rapid Cyclolysis Event

JONATHAN E. MARTIN AND NATHAN MARSILI

Department of Atmospheric and Oceanic Sciences, University of Wisconsin—Madison, Madison, Wisconsin

(Manuscript received 19 March 2001, in final form 26 October 2001)

ABSTRACT

Employing output from a successful numerical simulation, piecewise potential vorticity inversion is used to diagnose a rapid surface cyclolysis event that occurred south of the Aleutian Islands in late October 1996. The sea level pressure minimum of the decaying cyclone rose 35 hPa in 36 h as its associated upper-tropospheric wave quickly acquired a positive tilt while undergoing a rapid transformation from a nearly circular to a linear morphology. The inversion results demonstrate that the upper-tropospheric potential vorticity (PV) anomaly exerted the greatest control over the evolution of the lower-tropospheric height field associated with the cyclone.

A portion of the significant height rises that characterized this event was directly associated with a diminution of the upper-tropospheric PV anomaly that resulted from negative PV advection by the full wind. This forcing has a clear parallel in more traditional synoptic/dynamic perspectives on lower-tropospheric development, which emphasize differential vorticity advection. Additional height rises resulted from promotion of increased anisotropy in the upper-tropospheric PV anomaly by upper-tropospheric deformation in the vicinity of a southwesterly jet streak. As the PV anomaly was thinned and elongated by the deformation, its associated geopotential height perturbation decreased throughout the troposphere in what is termed here PV attenuation.

The analysis reveals that neither surface friction nor latent heat release played a primary role in this case of rapid surface decay. It is suggested, therefore, that rapid surface cyclolysis is unlikely to occur except in large-scale environments that promote rapid erosion of the upper-tropospheric PV anomalies associated with synoptic-scale short waves.

1. Introduction

Compared to the wealth of observational and modeling studies of the development, mature, and occluded stages of the midlatitude cyclone, almost no detailed case studies of cyclone decay have been undertaken. In Part I of this series of papers (Martin et al. 2001) the results of an 11-yr synoptic climatology of surface cyclolysis in the North Pacific Ocean were presented along with an analysis of the composite structure and evolution of cyclones experiencing rapid cyclolysis (i.e., filling rates greater than or equal to 12 hPa in 12 h). Based upon their composite analysis, the relative rarity of rapid cyclolysis, and the ubiquity of boundary layer friction in surface cyclone decay, they concluded that the distinguishing physical factor in *rapid* cyclolysis is the significant and abrupt decay of the upper-level trough-ridge structure. In order to both fortify these synoptic-climatological results and to develop a better understanding of the decay phase of the cyclone life cycle,

this paper presents a case study diagnosis of an observed rapid cyclolysis event.

One of the cyclones that contained a rapid cyclolysis period (RCP) in the climatology presented in Part I developed and decayed in the North Pacific Ocean, south of the Aleutian Islands, during the final week of October 1996. Though it did not exhibit the representative structure and evolution of the composite RCP from the climatology, this storm was a particularly robust example of rapid cyclolysis in that its minimum sea level pressure increased by 35 hPa in the 36 h from 0000 UTC 26 October to 1200 UTC 27 October. From among several storms that exhibited similarly extraordinary decay rates, this particular system was selected for detailed analysis because the storm center remained over the open ocean during the entire period of rapid decay. Presumably this characteristic served to minimize the influence of topography on the lower-tropospheric decay thus allowing the analysis to focus on the synoptic-scale processes in the free atmosphere to which the rapid cyclolysis might be ascribed.

Given that the cyclone of interest grew and decayed over the North Pacific Ocean, actual observations of it were not plentiful. For this reason, the centerpiece of our diagnosis is a numerical simulation of this cyclolysis

Corresponding author address: Dr. Jonathan E. Martin, Department of Atmospheric and Oceanic Sciences, University of Wisconsin—Madison, 1225 W. Dayton St., Madison, WI 53706.
E-mail: jon@meteor.wisc.edu

event performed using the Pennsylvania State University–National Center for Atmospheric Research (Penn State–NCAR) fifth-generation Mesoscale Model (MM5). Employing the gridded output from this successful simulation, a piecewise potential vorticity (PV) inversion was performed to determine the relative contributions of discrete pieces of the PV to the cyclone decay.

The paper is organized as follows. A synoptic description of the case is given in section 2. The details of the model simulation are described in section 3. In order to provide some evaluation of the veracity of the simulation, section 3 also includes some comparison of the model output to available surface and upper air analyses from the European Centre for Medium-Range Weather Forecasts (ECMWF) as well as to water vapor satellite imagery. A description of the piecewise inversion procedure along with a PV diagnosis of the rapid surface cyclolysis observed in this case is given in section 4. Discussion of the results is given in section 5. Section 6 follows with a summary and conclusions with suggestions for future work.

2. Synoptic evolution

The paucity of data in the North Pacific Ocean precludes a synoptic description that is based solely on observational data. Instead, we present the ECMWF uninitialized analyses as a proxy for the observations. These data come from a global analysis at 2.5° latitude–longitude horizontal resolution at 11 vertical levels: 1000, 850, 700, 500, 400, 300, 250, 200, 150, 100, and 50 hPa.

Geopotential height and virtual temperature data at 1000 hPa were used to estimate the sea level pressure at each grid point using the altimeter equation:

$$P_{sl} = 1000 \left(1 + \frac{\phi \Gamma}{g T_v} \right)^{g/RT}, \quad (1)$$

where ϕ is the geopotential at 1000 hPa, R is the gas constant for dry air, g is the acceleration due to gravity, T_v is the 1000-hPa virtual temperature, Γ is the standard atmospheric lapse rate, and P_{sl} is the pressure at sea level. We begin the synoptic overview at 1200 UTC 24 October 1996.

a. 1200 UTC 24 October

At 1200 UTC 24 October 1996 a surface cyclone of modest intensity was located just east of the date line (Fig. 1a). It had developed slowly beginning at ~1200 UTC 23 October and by this time had a clearly defined cold front trailing to its south while a broad baroclinic zone, characterized by warm air advection, was draped eastward through the downstream anticyclone. At 300 hPa a sharply curved short-wave trough, with a wind speed maximum on its eastern flank, was located just

upstream of the surface cyclone (Fig. 1b). The 300-hPa Q-vector divergence at this time revealed that the surface cyclone was located beneath a column characterized by significant quasigeostrophic forcing for ascent (Fig. 1c). Finally, the potential vorticity (PV) in the 300–250-hPa layer (located near the tropopause) demonstrated that a significant tropopause-level PV feature was associated with the developing surface cyclone (Fig. 1d).

b. 1200 UTC 25 October

Rapid development occurred in the ensuing 24 h as the surface cyclone of interest deepened to 966 hPa, its greatest intensity, by 1200 UTC 25 October. The frontal structure was robustly occluded by this time, as a significant ridge in the 1000–500-hPa thickness was evident (Fig. 2a). The short-wave disturbance at 300 hPa had also developed dramatically in this 24-h period. By 1200 UTC 25 October, its central geopotential height minimum had dropped by more than 140 m and it was located directly atop the sea level pressure minimum. The jet streak on its eastern flank had also intensified significantly by this time (Fig. 2b). This period of dramatic development was characterized by continued middle- and upper-tropospheric Q-vector convergence above the sea level cyclone though, at this time, the most significant forcing was displaced to the northeast of the sea level pressure minimum (Fig. 2c). The 300–250-hPa-layer-average PV at this time was characterized by a broad, high-amplitude trough–ridge couplet over the North Pacific basin, east of the date line (Fig. 2d).

c. 1200 UTC 26 October

During the 24-h period ending at 1200 UTC 26 October, the cyclone of interest began its remarkably rapid decay both at the surface and at upper levels.¹ The sea level pressure minimum by this time had filled to 986 hPa (12 hPa of filling occurring between 0000 and 1200 UTC) while a secondary sea level pressure minimum had developed at the peak of the original warm sector and had raced off to the northeast into the Gulf of Alaska (Fig. 3a). A remarkable transformation in the 300-hPa flow also occurred by this time as the slightly negatively tilted, tightly closed off geopotential height minimum had become an open, positively tilted, elongated geopotential trough axis (Fig. 3b). The jet streak on the eastern flank of the 300-hPa trough began to acquire a slight anticyclonic curvature and continued to intensify as it elongated. Also, the dramatic pressure rise at sea level was attended by a 300-hPa geopotential height rise

¹ Though other measures can be employed to assess decay [e.g., Sinclair (1997) advocates using circulation], we use minimum sea level pressure as our proxy for intensity throughout the analysis.

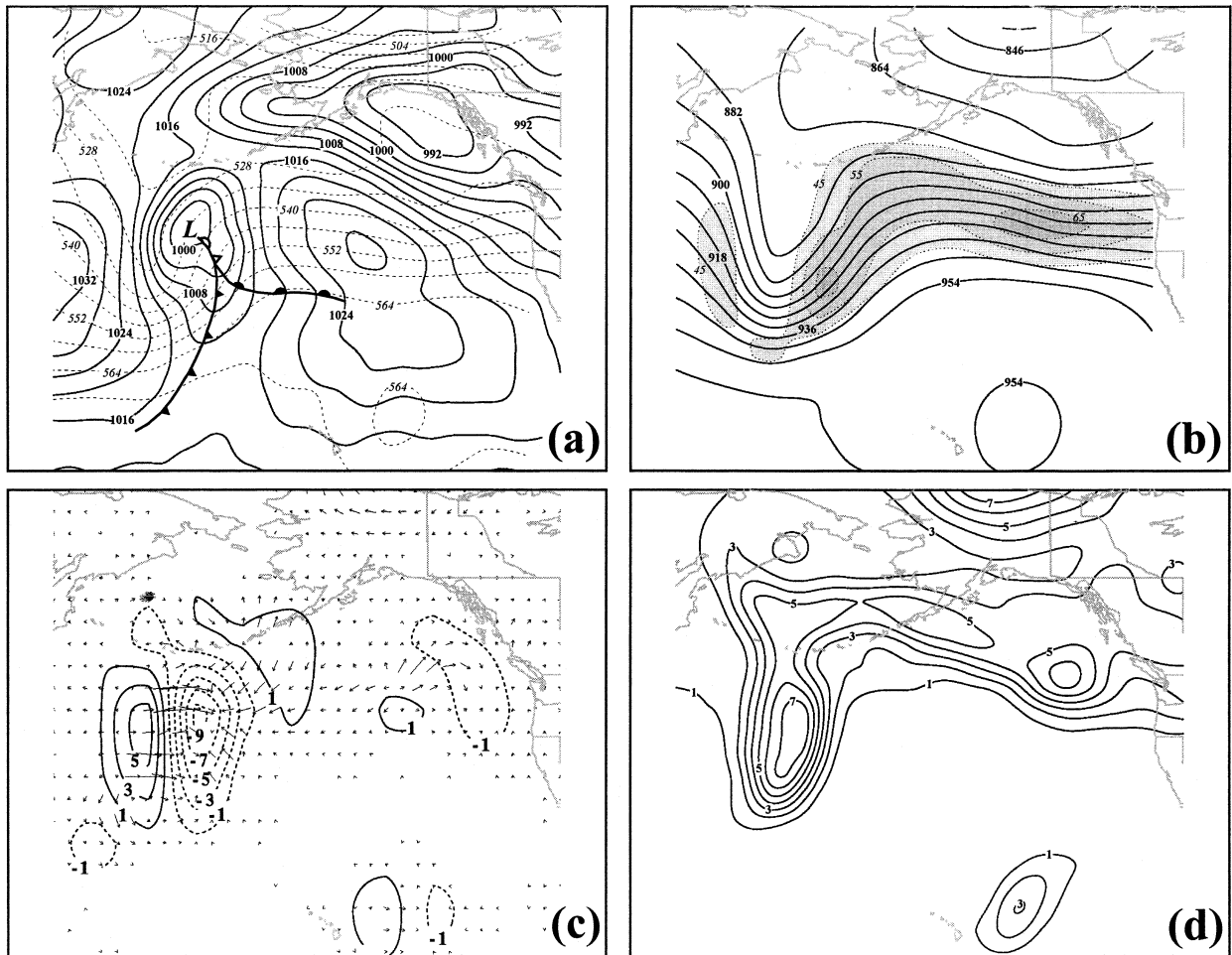


FIG. 1. (a) Mean sea level pressure (solid lines) and 1000–500-hPa thickness (dashed lines) from the ECMWF TOGA analysis at 1200 UTC 24 Oct 1996. Mean sea level pressure is labeled in hPa and contoured every 4 hPa. The 1000–500-hPa thickness is labeled in dm and contoured every 6 dm. Surface fronts are indicated by traditional frontal symbols. (b) The 300-hPa geopotential height (solid lines) and isotachs (shaded) from the ECMWF TOGA analysis at 1200 UTC 24 Oct 1996. Geopotential height is labeled in dm and contoured every 9 dm. Isotachs are labeled in m s^{-1} and shaded every 10 m s^{-1} beginning at 45 m s^{-1} . (c) The 300-hPa Q vectors and Q-vector forcing for ω ($-2\nabla \cdot \mathbf{Q}$) from the ECMWF TOGA analysis at 1200 UTC 24 Oct 1996. Solid (dashed) lines are Q-vector divergence (convergence) labeled in $\text{m kg}^{-1} \text{ s}^{-1}$ and contoured every $2 (-2) \times 10^{-15} \text{ m kg}^{-1} \text{ s}^{-1}$ beginning at $1 (-1) \times 10^{-15} \text{ m kg}^{-1} \text{ s}^{-1}$. (d) The 300–250-hPa column-averaged PV from the ECMWF TOGA analysis at 1200 UTC 24 Oct 1996; PV is labeled in PVU ($1 \text{ PVU} = 10^{-6} \text{ m}^2 \text{ K kg}^{-1} \text{ s}^{-1}$) and contoured every 1 PVU beginning at 1 PVU.

of $\sim 100 \text{ m}$ directly above the sea level pressure minimum.

Associated with the dramatic change in the upper-tropospheric structure as decay began was the sudden reduction in significant Q-vector convergence above the surface low by 1200 UTC 26 October (Fig. 3c). The surface cyclone was thus abruptly stripped of one of its major developmental forcings at this time. Reflecting the rapid transformation in the upper-tropospheric structure, the 300–250-hPa-layer-average PV feature acquired a positive tilt as well (Fig. 3d). Notice also that the PV maxima was reduced to 7 PVU ($1 \text{ PVU} = 10^{-6} \text{ m}^2 \text{ K kg}^{-1} \text{ s}^{-1}$) by this time, indicative of a retreat of the tropopause to lower pressures during decay.

d. 1200 UTC 27 October

Finally, by 1200 UTC 27 October, the sea level pressure minimum had filled another 25 hPa to 1011 hPa completing a remarkable filling of 35 hPa in 36 h. All that remained of the originally robust frontal structure was a substantial, elongated cold frontal baroclinic zone stretching from southeast of the primary sea level pressure minimum to northwest of Hawaii (Fig. 4a). The 300-hPa trough associated with the primary surface cyclone was positioned between two high-amplitude, positively tilted ridge axes by this time (Fig. 4b). Very little quasigeostrophic (QG) forcing for ω was evident at this time (Fig. 4c) and the 300–250-hPa PV reflected con-

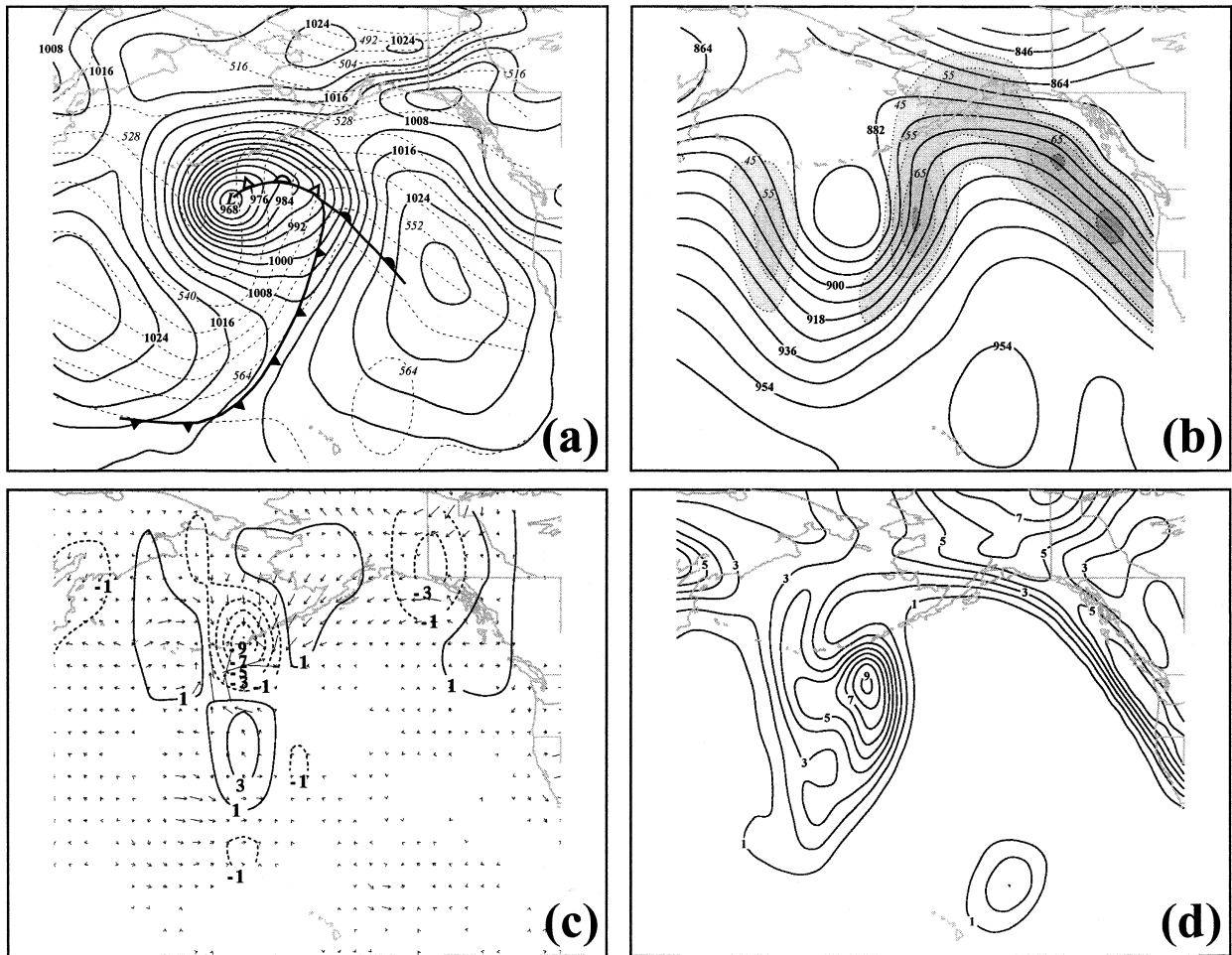


FIG. 2. (a) As for Fig. 1a but for 1200 UTC 25 Oct 1996. (b) As for Fig. 1b but for 1200 UTC 25 Oct 1996. (c) As for Fig. 1c but for 1200 UTC 25 Oct 1996. (d) As for Fig. 1d but for 1200 UTC 25 Oct 1996.

tinued thinning of the high-latitude PV filament (Fig. 4d). Over this entire 3-day evolution, the upper-tropospheric flow and tropopause-level PV evolved in much the same manner as the LC1 life cycle described by Thorncroft et al. (1993).

3. Model description

In order to perform the piecewise potential vorticity diagnosis of this case, we use gridded output from a successful numerical simulation of the event performed using version 3 of the Penn State–NCAR MM5 described by Grell et al. (1994). The model employs a one-way nested grid with a coarse outer domain (grid 1) and a finer-scale inner domain (grid 2) with horizontal resolutions of 100 and 50 km, respectively, projected onto a Lambert conformal grid (Fig. 5). The ECMWF Tropical Ocean Global Atmosphere (TOGA) analyses, at $2.5^\circ \times 2.5^\circ$ latitude–longitude resolution, were used to initialize the model. Grid 1 boundary conditions were updated every 12 h with these data while the grid 2

boundaries were updated every 2 h with the output from the grid 1 simulation.

Model physics include a cloud-sensitive radiation scheme, a mixed-phase precipitation scheme, as well as a five-layer predictive soil model (Dudhia 1996). The boundary layer scheme developed by Hong and Pan (1996) was implemented along with the Grell (1993) cumulus parameterization. The model employed a terrain-following sigma (σ) coordinate system and 23 half- σ levels were used in the simulation. This output was interpolated to 20 isobaric levels at 50-hPa intervals from 1000 to 50 hPa. The object simulation was initialized at 1200 UTC 25 October 1996 and was run for 48 h.

A systematic evaluation of the model simulation will not be presented here though, in Figs. 6 and 7, we offer a limited verification. The sea level pressure and 1000–500-hPa thickness forecasts at 12-h intervals from 0000 UTC 26 October to 1200 UTC 27 October are shown in Fig. 6. The simulated fields at 1200 UTC 26 October (Fig. 6b) and 1200 UTC 27 October (Fig. 6d) compare very well with the corresponding ECMWF analyses pre-

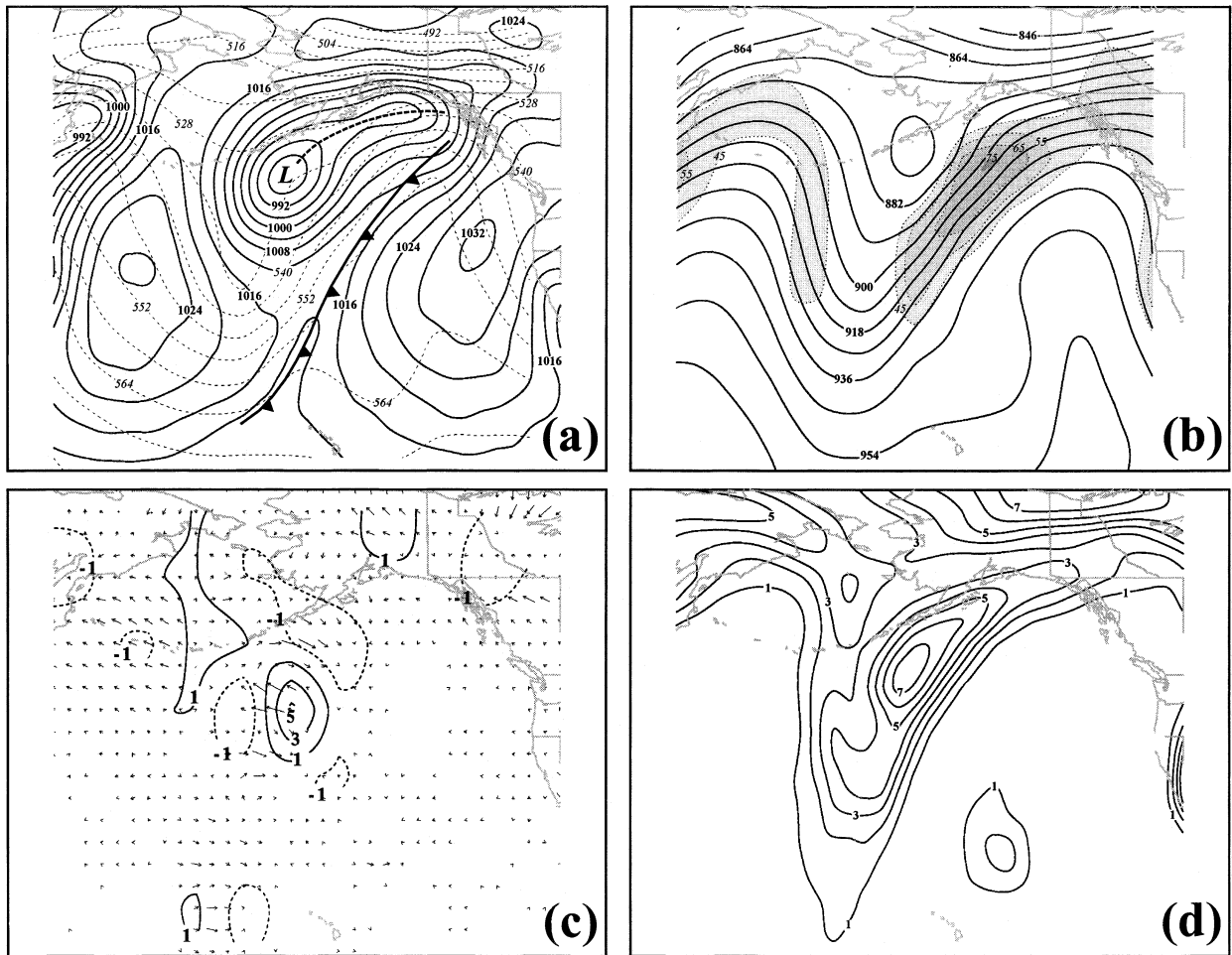


FIG. 3. (a) As for Fig. 1a but for 1200 UTC 26 Oct 1996. Dashed line indicates sea level pressure trough. (b) As for Fig. 1b but for 1200 UTC 26 Oct 1996. (c) As for Fig. 1c but for 1200 UTC 26 Oct 1996. (d) As for Fig. 1d but for 1200 UTC 26 Oct 1996.

sented in Figs. 3a and 4a. The 300–250-hPa column-average PV from the model simulation along with Geostationary Operational Environmental Satellite (GOES) water vapor imagery over the North Pacific at three different times are shown in Fig. 7. The forecasted PV nicely fits the distribution of column-integrated water vapor with large (small) PV in relatively dry (moist) air. The forecast valid at 1200 UTC 26 October (Fig. 7b) compares reasonably well to the ECMWF analyses at the corresponding time (shown in Fig. 3d) although there are some notable differences. Perhaps most significant among these is the axis of low PV along the Alaska Peninsula and Aleutian Islands in the simulation that is only hinted at in the ECMWF analysis. Despite such discrepancies, the simulation was quite good. Specifically, the surface cyclolysis was faithfully replicated in the simulation as the sea level pressure minimum filled by 33.1 hPa in the 36 h from 1800 UTC 25 October to 0600 UTC 27 October. Given this accuracy, we confidently employ the gridded output from this simulation to perform a piecewise PV inversion in order to deter-

mine the relative contributions of discrete pieces of the PV to the rapid decay observed in this case.

4. Piecewise potential vorticity analysis

a. Technique and definitions

The Ertel potential vorticity (EPV) was first defined by Rossby (1940) and Ertel (1942) as

$$\text{EPV} = \frac{1}{\rho} \boldsymbol{\eta} \cdot \nabla \theta, \quad (2)$$

where ρ is the density, $\boldsymbol{\eta}$ the absolute vorticity vector, and θ the potential temperature. EPV is the potential vorticity for the complete atmospheric system; thus, it is conserved under the full primitive equations, given adiabatic, inviscid flow.

The goal of piecewise PV inversion is to recover the mass and momentum fields associated with discrete PV anomalies. The success of this endeavor, and therefore the usefulness of the resulting information, is limited

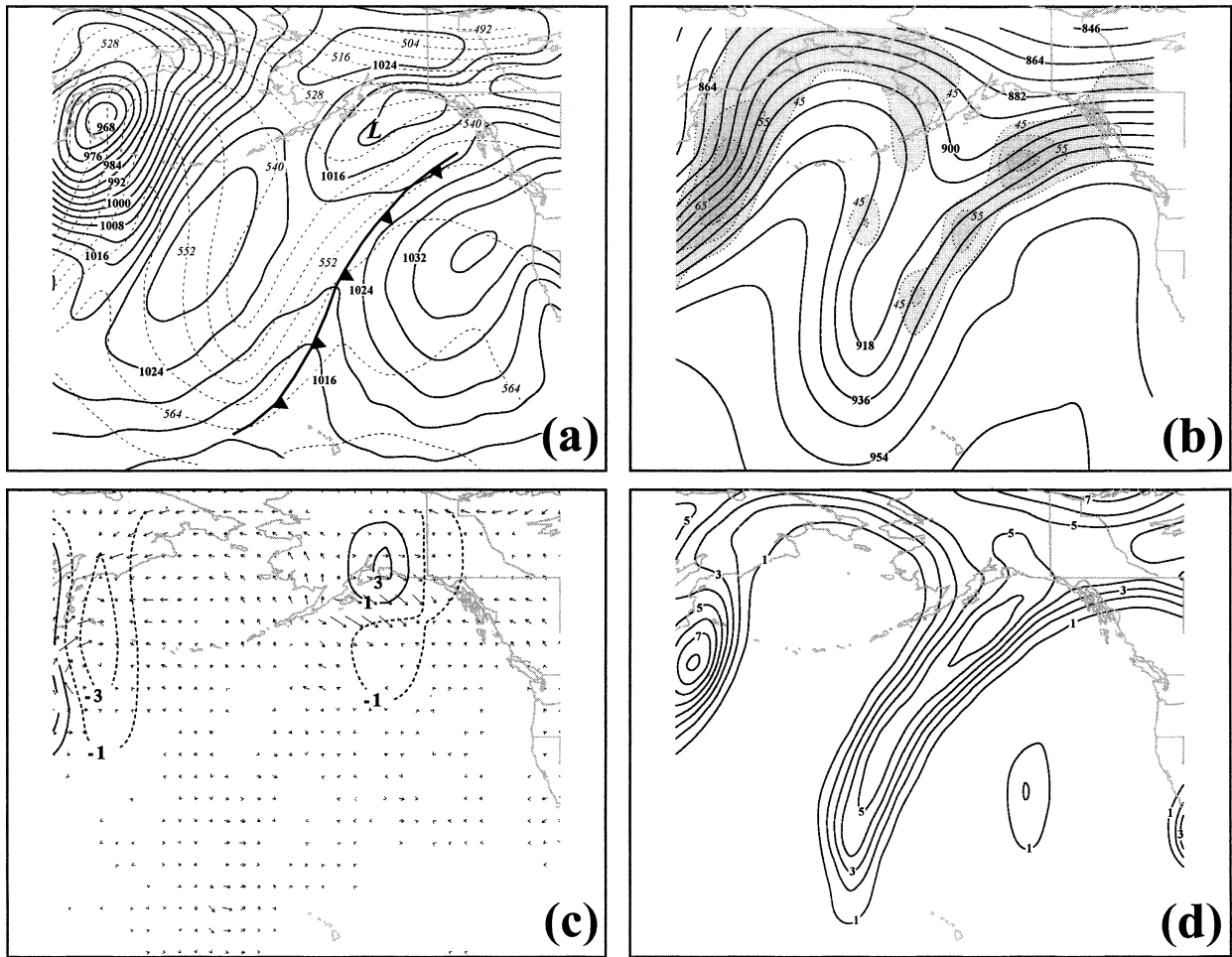


FIG. 4. (a) As for Fig. 1a but for 1200 UTC 27 Oct 1996. (b) As for Fig. 1b but for 1200 UTC 27 Oct 1996. (c) As for Fig. 1c but for 1200 UTC 27 Oct 1996. (d) As for Fig. 1d but for 1200 UTC 27 Oct 1996.

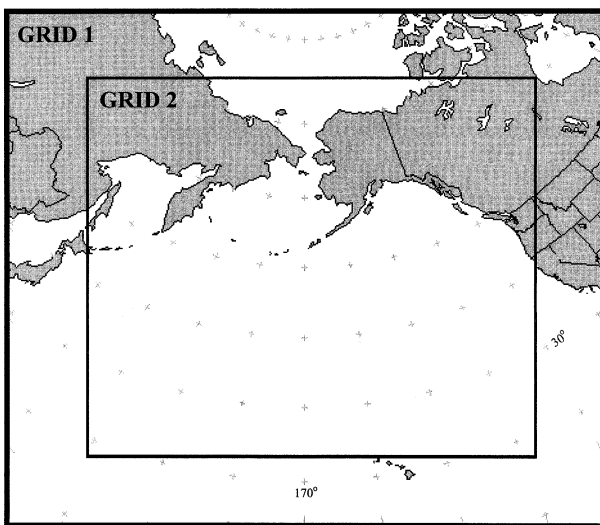


FIG. 5. Inner (grid 2) and outer (grid 1) domains of the MM5 simulation used in this analysis. The plus (+) symbols indicate lat-lon intersections at 10° intervals.

by the approximations made to obtain a balanced system. The Davis and Emanuel (1991, hereafter DE) inversion method, which is employed in this study, assumes 1) hydrostatic balance, and 2) that the magnitude of the irrotational component of the wind is much smaller than the magnitude of the nondivergent component (i.e., $|\mathbf{v}_\chi| \ll |\mathbf{v}_\psi|$). Applying these approximations to the divergence equation and (2) results in the invertibility statement for this system (DE):

$$\nabla^2\Phi = \nabla \cdot (f\nabla\psi) + \frac{2}{a^4 \cos^2\phi} \frac{\partial}{\partial \lambda} \left(\frac{\partial\psi}{\partial\lambda}, \frac{\partial\psi}{\partial\phi} \right) \quad (3)$$

$$\text{EPV} = \frac{g\kappa\pi}{P} \left[(f + \nabla^2\psi) \frac{\partial^2\Phi}{\partial\pi^2} - \frac{1}{a^2 \cos^2\phi} \frac{\partial^2\psi}{\partial\lambda\partial\pi} \frac{\partial^2\Phi}{\partial\lambda\partial\pi} - \frac{1}{a^2} \frac{\partial^2\psi}{\partial\phi\partial\pi} \frac{\partial^2\Phi}{\partial\phi\partial\pi} \right], \quad (4)$$

where Φ is the geopotential, ψ is the nondivergent

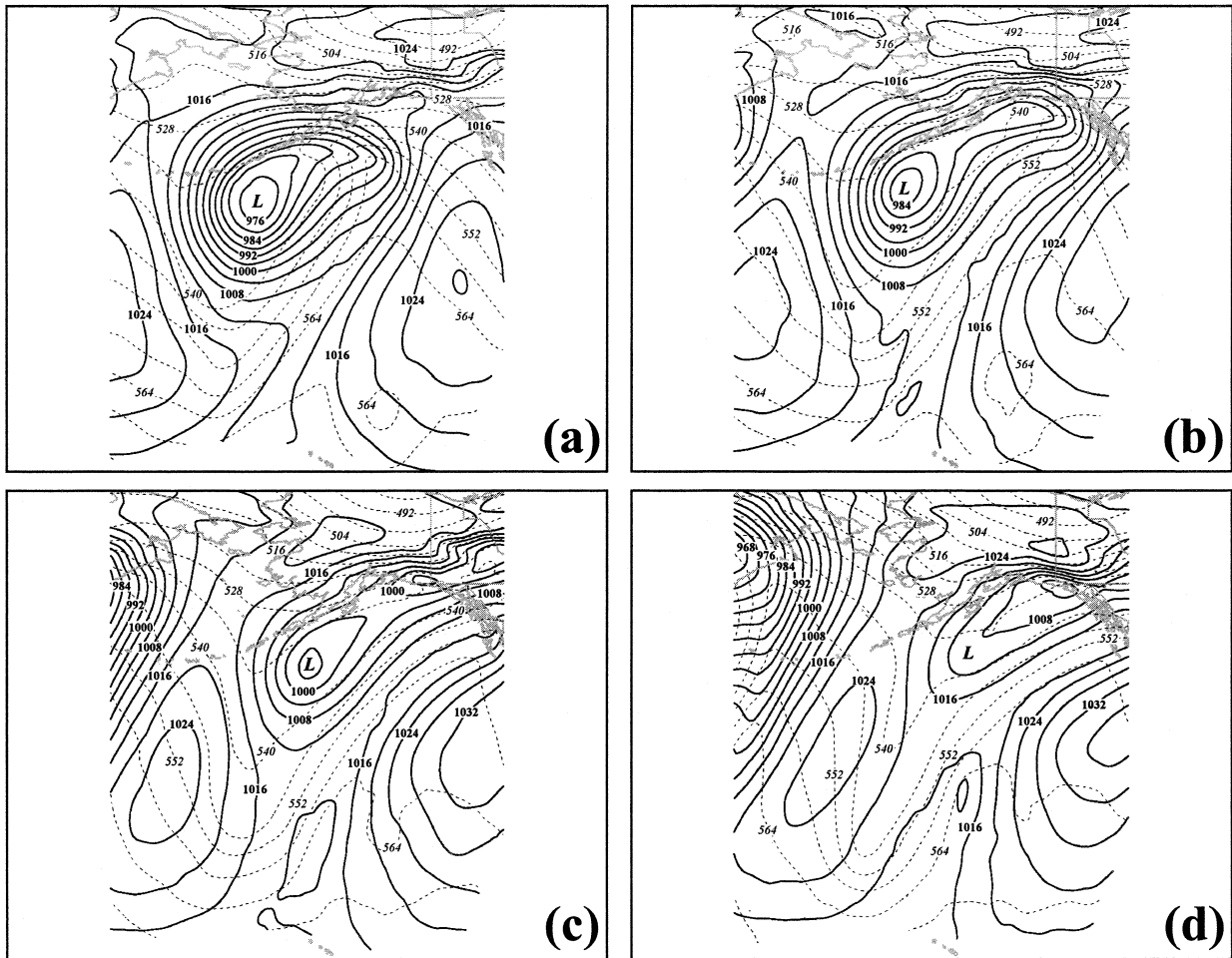


FIG. 6. (a) MM5 12-h forecast of mean sea level pressure (solid lines) and 1000–500-hPa thickness (dashed lines) valid at 0000 UTC 26 Oct 1996. Mean sea level pressure is labeled in hPa and contoured every 4 hPa. The 1000–500-hPa thickness is labeled in dm and contoured every 6 dm. (b) As in (a) but a 24-h forecast valid at 1200 UTC 26 Oct 1996. (c) As in (a) but a 36-h forecast valid at 0000 UTC 27 Oct 1996. (d) As in (a) but a 48-h forecast valid at 1200 UTC 27 Oct 1996.

streamfunction, λ is the longitude, ϕ is the latitude, a is the radius of the earth, $\kappa = R/c_p$, P is pressure, and π is the Exner function [$c_p(p/p_0)^\kappa$], which serves as the vertical coordinate. Equation (3) is the Charney nonlinear balance equation (Charney 1955), which has been shown by prior studies to be an excellent approximation to observed flows (e.g., Davis et al. 1996), thus, validating the application of PV diagnostics to the real atmosphere. Careful comparison of the model winds and the computed nondivergent balanced winds for the present case demonstrates that differences exist where expected (such as in trough and ridge axes and in association with wind speed maxima).

Using PV computed from the model's wind and temperature fields at all vertical levels over grid 2, a total inversion is performed, solving this system of two equations simultaneously for ψ and Φ , with ψ and Φ prescribed on the lateral boundaries and their vertical derivatives specified on the top and bottom boundaries. The potential temperature at 975 and 75 hPa provides

these Neumann boundary conditions on the horizontal boundaries. Also, negative values of PV are set to a small positive constant value (0.01 PVU). For a complete description of the boundary conditions, as well as the numerical methods used to solve the system of equations, the reader is referred to DE.

In order to perform piecewise PV inversion, mean and perturbation fields must be defined. We employed a time mean by considering a 144-h time window composed of three consecutive 48-h simulations; one initialized at 1200 UTC 23 October, the object run described in section 2, and another initialized at 1200 UTC 27 October. All three simulations were run in the manner described in section 2. Employing the output from these three simulations, a 144-h time mean was constructed. The objective in computing such a mean is to isolate the features of interest in the PV field, thus placing them solely in the perturbation field. Once this time mean was computed, it was subtracted from the instantaneous PV distribution at each discrete time in

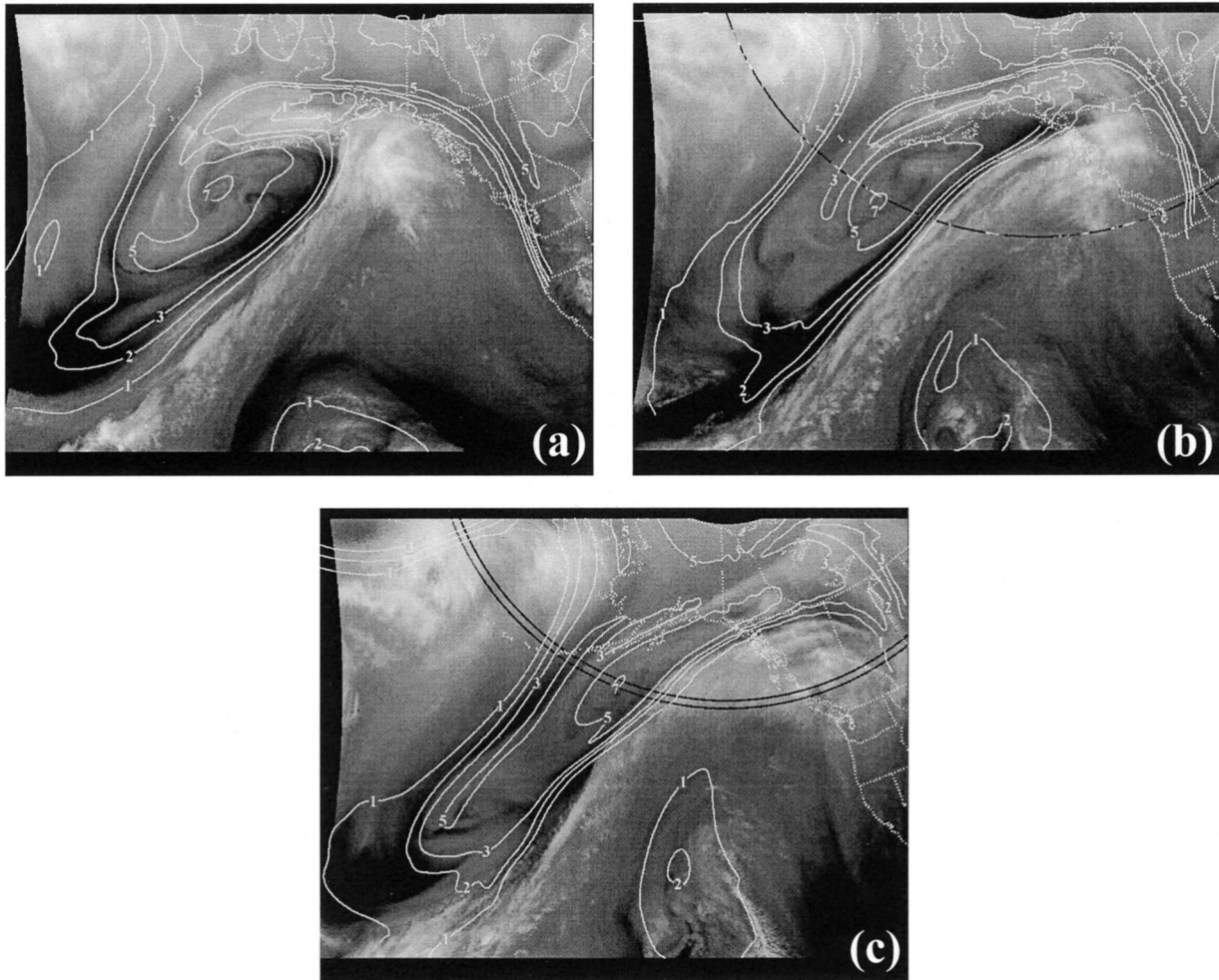


FIG. 7. (a) MM5 12-h forecast of 300–250-hPa column-averaged PV (thick white lines) superimposed on *GOES-9* 6.7- μm water vapor imagery at 0000 UTC 26 Oct 1996. Column-averaged PV is labeled in PVU with 1, 2, 3, 5, and 7 PVU values contoured. (b) As for (a) but using a 24-h MM5 forecast valid at 1200 UTC 26 Oct 1996. (c) As for (a) but using a 36-h MM5 forecast valid at 0000 UTC 27 Oct 1996.

the object run. The difference between the time mean and the instantaneous PV is referred to as the perturbation PV for that time.

Effective use of piecewise potential vorticity inversion requires a meaningful partitioning of the perturbation PV. The goals of partitioning are 1) to account for nearly all of the perturbation PV, while not inverting any of it more than once, and 2) to select the minimum number of partitions that adequately describe the features in question. One way to accomplish these goals is by grouping together potential vorticity anomalies with a common history (Davis 1992). We therefore adopt a conventional three-way partitioning involving an upper layer, an interior layer, and a surface layer similar to that employed by Korner and Martin (2000).

The upper layer extends from 650 to 50 hPa and is designed to isolate PV anomalies associated with undulations in the tropopause. In order to consider only

upper-tropospheric/lower-stratospheric air in this category, we set the positive perturbation PV in this layer to 0.0 PVU whenever the relative humidity was greater than or equal to 70%.² The method retains *all* negative perturbation PV in this layer, thereby preventing the elimination of upper-level downstream ridges, which often exist in moist air.

The interior layer extends from 950 to 400 hPa and is designed to isolate midtropospheric PV anomalies associated with latent heat release. Given that such latent heat release will occur in an environment at or near saturation, the PV in this layer is set to 0.0 PVU when-

² Careful examination of the output showed that air with $\text{RH} \geq 70\%$ contained only a negligibly small portion of the total positive perturbation PV in the 650–50-hPa layer. Thus, for completeness, this air was eventually retained as a part of the upper-layer perturbation PV.

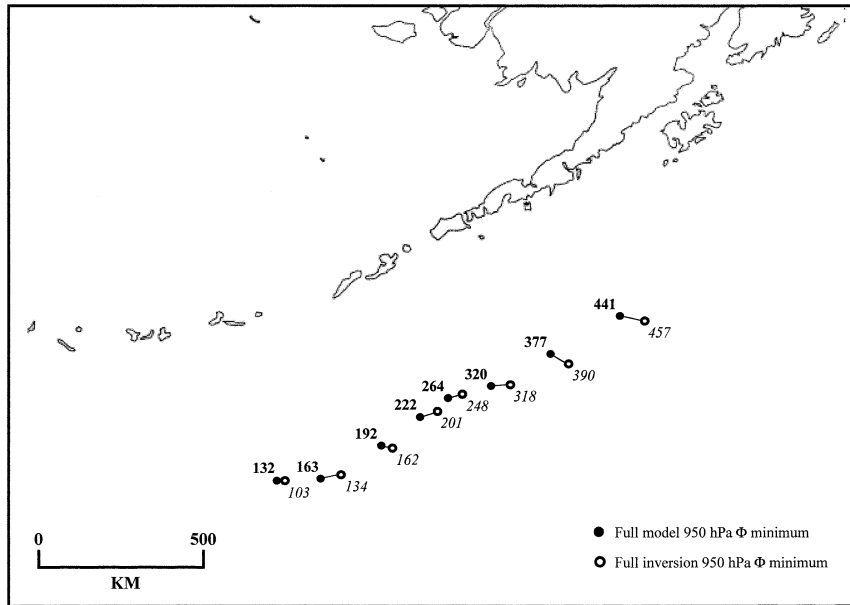


FIG. 8. The 6-hourly locations of the 950-hPa geopotential height minima from the MM5 forecasts (filled circles) compared to those obtained from inversion of the full perturbation PV field (open circles) from 0 to 42 h in the model forecast. Magnitude of the model (full inversion) 950-hPa geopotential height minima are given by bold (italicized) numbers adjacent to dots.

ever the relative humidity is less than 70%. This guards against the scheme mistaking extruded stratospheric perturbation PV for perturbation PV “produced” by latent heat release.

Finally, the surface layer extends from 950 to 850 hPa and also includes the 975-hPa potential temperature. This layer is designed to isolate the boundary potential temperature anomalies that are equivalent to PV anomalies just above the surface (Bretherton 1966). The surface layer, however, also includes perturbation PV in the 950–850-hPa layer. To ensure against redundancy with the interior layer, we set the perturbation PV in the 950–850-hPa layer to 0.0 PVU whenever the relative humidity is greater than or equal to 70%.

The combination of the three layers and their respective relative humidity criteria excludes only one part of the total perturbation PV distribution from being inverted, namely, perturbation PV in air with relative humidity less than 70% in the 800–700-hPa layer. Careful scrutiny of the data, however, revealed that this portion of the total perturbation PV distribution was very small in the present case. Finally, the potential double inversion of negative perturbation PV in air with relative humidity greater than or equal to 70% between 650 and 400 hPa was avoided by inverting this PV as a component of the interior layer only. For the remainder of the paper \mathbf{U}_{pert} will refer to perturbations associated with the upper layer, \mathbf{M}_{pert} to perturbations associated with the interior layer, and \mathbf{S}_{pert} to perturbations associated with the surface layer.

b. Evaluation

Once the inversion was performed, the effect of each of the three pieces of perturbation PV on the lower-tropospheric height changes during rapid cyclolysis was considered. Since 950 hPa was the lowest available isobaric surface in the inversion output, subsequent analysis will concentrate on the evolution of geopotential height at that level. The location and intensity of the 950-hPa PV inversion height minima are compared to the model 950-hPa height minima in Fig. 8. The inversion heights are lower than the model heights initially (i.e., when the cyclone is strong) and then larger than the model heights at the end of the decay. It is also clear from Fig. 8 that the model and inversion height minima are nearly geographically coincident throughout the rapid decay.

c. Partitioned height changes

Figure 9 shows the 950-hPa height anomalies associated with the \mathbf{U}_{pert} PV anomaly at 12-h intervals from 0000 UTC 26 October to 0000 UTC 27 October (the 24-h period of most rapid cyclolysis). The L in Fig. 9 represents the position of the 950-hPa height minimum obtained from inversion of the full perturbation PV field at each respective time. It is clear from Fig. 9 that the height perturbation associated with the \mathbf{U}_{pert} PV anomaly weakens considerably over this 24-h period. In order to make an eventual comparison between the partitioned height changes and the full model height changes, we

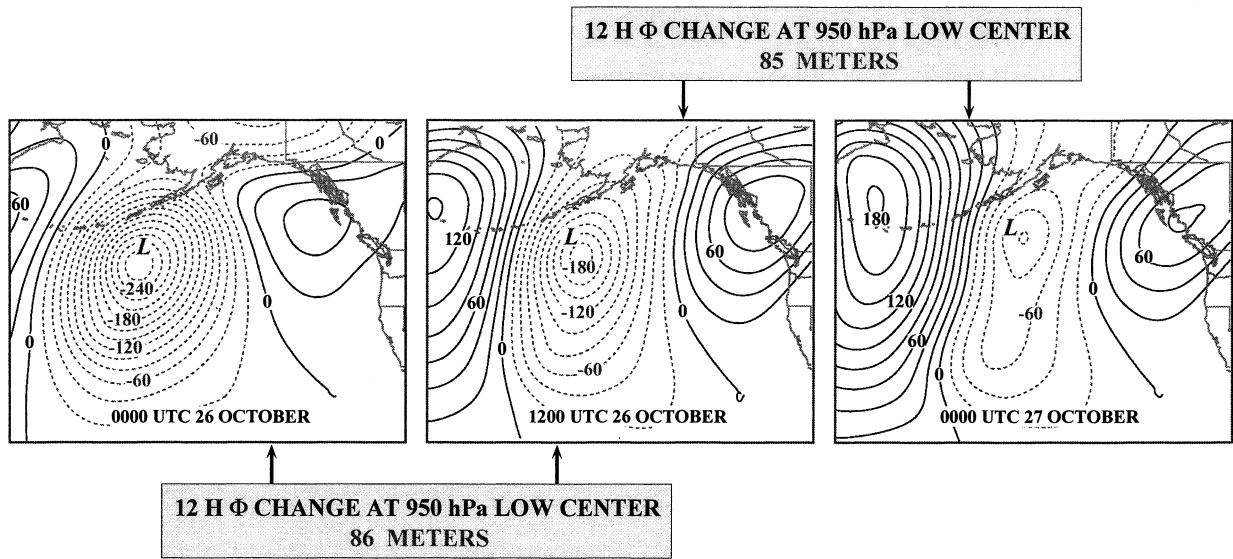


FIG. 9. (a) The 950-hPa geopotential height perturbation associated with the U_{pert} PV anomaly at 0000 UTC 26 Oct 1996. Negative (positive) geopotential height perturbations are indicated by dashed (solid) lines and contoured every 20 m. The L indicates position of the 950-hPa full inversion geopotential height minimum at 0000 UTC 26 Oct 1996. (b) As for (a) but for 1200 UTC 26 Oct 1996. (c) As for (a) but for 0000 UTC 27 Oct 1996.

evaluated the change in perturbation height *at the position of the full inversion height minimum* (i.e., the L) between successive 12-h periods. The results in Fig. 9 show that height rises of the same magnitude (~ 85 m), associated with changes in the U_{pert} height perturbations, occurred in both 12-h periods.

A similar analysis of the height changes associated with the S_{pert} PV anomaly is shown in Fig. 10. In the first 12-h period a modest rise of 10 m occurred as the

S_{pert} height perturbation minimum remained nearly stationary but decreased in magnitude. In the subsequent 12-h period, a 47-m height rise occurred as the -120 m perturbation height contour migrated northeastward toward southeastern Alaska. Synoptically, this was related to the rapid northeastward migration of the peak of the original warm sector away from the decaying surface cyclone; a behavior characteristic of deeply occluded cyclones.

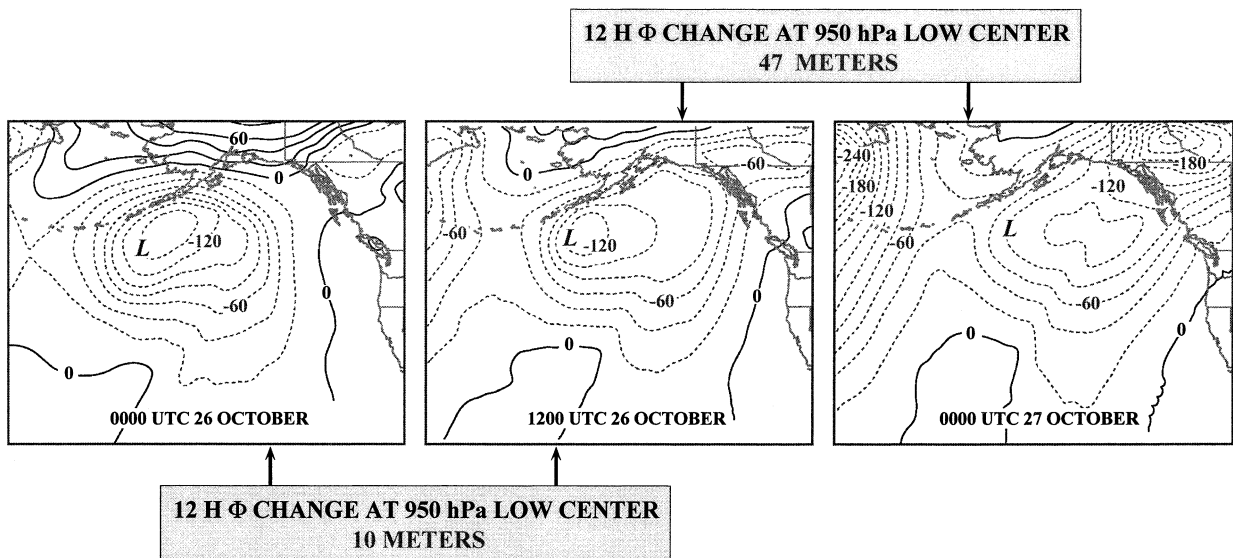


FIG. 10. (a) The 950-hPa geopotential height perturbation associated with the S_{pert} PV anomaly at 0000 UTC 26 Oct 1996. Negative (positive) geopotential height perturbations are indicated by dashed (solid) lines labeled in m and contoured every 20 m. The L indicates position of the 950-hPa full inversion geopotential height minimum at 0000 UTC 26 Oct 1996. (b) As for (a) but for 1200 UTC 26 Oct 1996. (c) As for (a) but for 0000 UTC 27 Oct 1996.

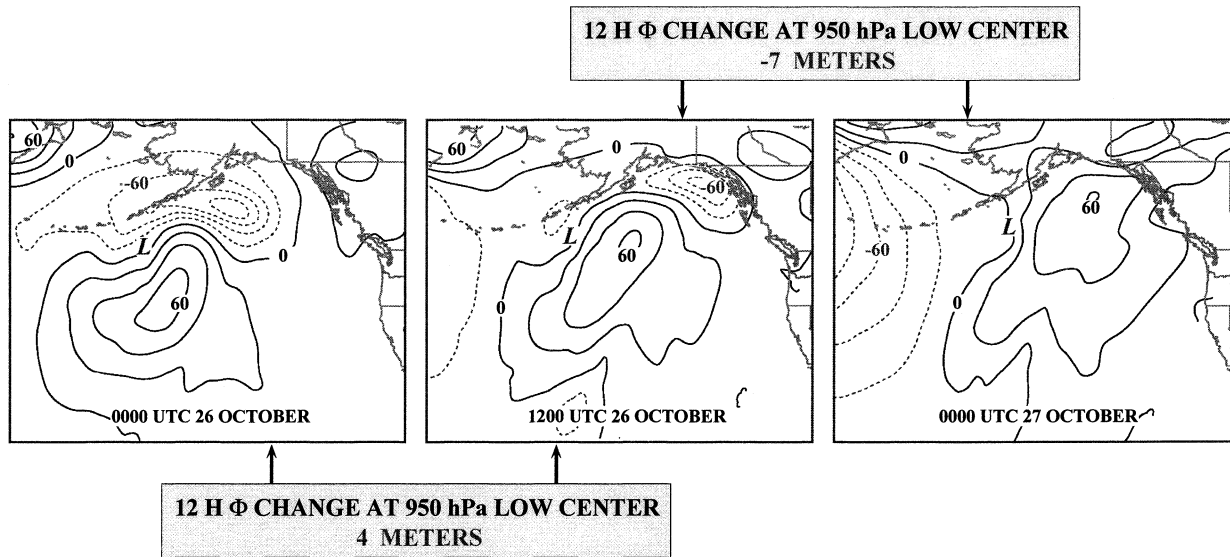


FIG. 11. (a) The 950-hPa geopotential height perturbation associated with the M_{pert} PV anomaly at 0000 UTC 26 Oct 1996. Negative (positive) geopotential height perturbations are indicated by dashed (solid) lines labeled in m and contoured every 20 m. The L indicates position of the 950-hPa full inversion geopotential height minimum at 0000 UTC 26 Oct 1996. (b) As for (a) but for 1200 UTC 26 Oct 1996. (c) As for (a) but for 0000 UTC 27 Oct 1996.

One means of assessing a cyclolytic effect of latent heat release is by considering the height perturbations associated with the M_{pert} PV anomaly (Fig. 11). The strong latent heat release associated with the warm and occluded frontal regions of this cyclone³ as decay commenced is manifest as a negative height perturbation located south-southeast of Kodiak Island at 0000 UTC 26 October (Fig. 11a). By 1200 UTC 26 October, that height minimum feature had raced off to the northeast (Fig. 11b) and was directly associated with the formation of the weak secondary surface cyclone that developed at the peak of the original warm sector. That feature was not long lived, however, as no trace of it was evident just 12 h later (Fig. 11c). Most importantly, the M_{pert} height changes at the location of the primary cyclone were negligibly small. In fact, the M_{pert} PV anomaly associated with the robust *upstream* development may have induced the weak height falls at the primary low center in the 12 h ending at 0000 UTC 27 October (Fig. 11c).

Finally, Fig. 12 offers a summary of the 6-hourly evolution of height changes at the 950-hPa geopotential height minimum. The total nondivergent partitioned perturbation height changes compare well in magnitude and tendency to those derived from the full model simulation (Fig. 12a). Upon partitioning the total nondivergent perturbation height changes into contributions from the three pieces, it is clear that the U_{pert} height changes are the most significant contributors to the total height

changes. The S_{pert} contribution is usually a distant second, the exception being the 6-h interval from 1200 to 1800 UTC 26 October wherein the two are comparable (Fig. 12b). Interestingly, the M_{pert} contribution to height changes at the geopotential minimum oscillates about 0, suggesting there is never any significant impact of M_{pert} geopotential height perturbations on the rapid surface cyclolysis observed in this case.

Thus, the preceding analysis suggests that the tropopause-level PV anomaly exerted the greatest control on the rapid cyclolysis observed in this case. We next consider the physical factors that conspired to produce the height rises associated with the U_{pert} PV anomaly.

d. Tropopause-level PV evolution

The effect of a tropopause-level PV anomaly on lower-tropospheric heights is dependent on the scale, magnitude, and shape of the anomaly and is modulated by the intervening stratification (Hoskins et al. 1985). Figure 13 portrays the 300–250-hPa column-average perturbation PV superimposed upon the 950-hPa U_{pert} height anomalies at 12-h intervals from 0000 UTC 26 October 0000 UTC 27 October. Over this time period a significant reduction in the magnitude, along with a thinning and an elongation, of the perturbation PV occurred.

Vertical cross sections through the U_{pert} PV maxima at the same three times, along with the corresponding U_{pert} geopotential height anomalies are shown in Fig. 14. In the first 12-h period the U_{pert} PV decreases by more than 1 PVU from maximum values of greater than 6 PVU (Fig. 14a) to just over 5 PVU (Fig. 14b). In the second 12-h period, the U_{pert} PV does not experience as

³ Comparison of the object simulation to a companion “fake dry” simulation (not shown) suggests that it is this heating that likely played a significant role in producing the tropopause PV minimum north of the Aleutian Islands shown in Fig. 7.

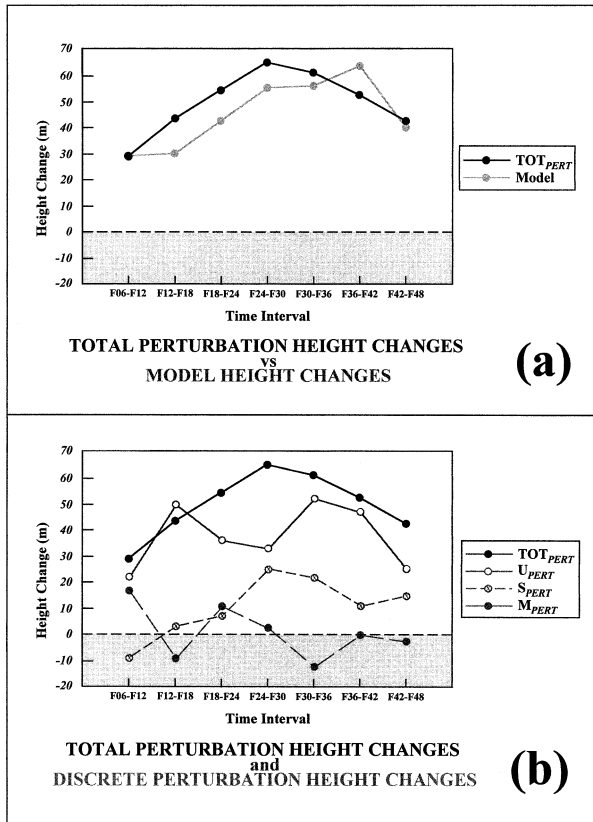


FIG. 12. (a) The 6-hourly height changes at the position of the 950-hPa geopotential height minimum from the full MM5 solution (light dots) and the sum of the partitioned perturbation heights (dark dots). (b) The 6-hourly height changes at the position of the 950-hPa geopotential height minimum from the sum of the partitioned perturbation heights (dark dots) and the three discrete perturbation heights (lighter dots). See text for explanation.

significant a decrease in magnitude. Note that at each of these three times the maximum U_{pert} PV is contained within the 350–300-hPa layer. Not surprisingly, this same layer exhibits the largest perturbation geopotential height at each time as well. Corresponding to the decrease in the U_{pert} PV there is a steady increase in the minimum geopotential height perturbation, from ~ -368 m at 0000 UTC 26 October (Fig. 14a) to slightly more than -180 m 24 h later (Fig. 14c).

Changes in the penetration depth of the U_{pert} PV anomaly can be assessed by comparing the ratio of the 950 to 350-hPa perturbation height minima at each time. At 0000 UTC 26 October, this ratio is 0.75 ($-275/-368$). In the next 24 h the ratio decreases steadily to 0.65 at 1200 UTC 26 October and further to 0.55 at 0000 UTC 27 October. Thus, the penetration depth of the U_{pert} PV anomaly decreases 27% over the period of rapid cyclolysis. Coincident with this change, the Brunt–Väisälä frequency (N) beneath the PV anomaly (in the 950–350-hPa layer) increases modestly (from 0.0117 s $^{-1}$ to 0.0124 s $^{-1}$) in the first 12 h and not at all in the subsequent 12 h. Thus, the decrease in penetration depth

is predominantly a result of changes in the magnitude and morphology of the U_{pert} PV anomaly.⁴

Figure 14 makes it clear that the substantial reduction of the U_{pert} PV maximum from 0000 to 1200 UTC 26 October was a major contributing factor to the rapid surface cyclolysis in that 12-h period. Some insight into the physical circumstances responsible for this diminution arises from consideration of the conservation principle for PV. As shown in Fig. 7, the maximum upper-tropospheric PV (which is coincident with the maximum U_{pert} PV) was far from the cloud shield associated with this storm throughout the 24-h period of most rapid surface decay. Calculations of the PV tendency resulting from latent heat release (LHR) for this case were made following Raymond (1992) and Cammas et al. (1994), employing a formulation of the diabatic heating rate developed by Emanuel et al. (1987). Consistent with inferences based on the satellite data, these calculations (not shown) indicated that LHR-induced PV tendencies were not present in the vicinity of the U_{pert} PV maximum during the 24-h period of most rapid surface cyclolysis. Thus, PV advection largely accounted for any local change in PV according to

$$\frac{d(\text{PV})}{dt} = 0 = \frac{\partial(\text{PV})}{\partial t} + \mathbf{V} \cdot \nabla(\text{PV}). \quad (5)$$

In this study, the full PV is made up of a time-mean and three partitioned perturbations, only one of which (U_{pert}) has any magnitude in the 300–250-hPa layer. As there can be no Eulerian change in the time-mean PV, (5) reduces to

$$\frac{\partial(\text{PV}_{U_{\text{pert}}})}{\partial t} = -\mathbf{V} \cdot \nabla(\text{PV}). \quad (6)$$

This relationship states that, in the absence of nonconservative processes, local changes in the 300–250-hPa U_{pert} PV anomaly at any time are forced by the full wind advection of the full PV at that time and in that layer. Figure 15 shows the 300–250-hPa column-averaged horizontal PV advection overlaid upon the 300–250-hPa U_{pert} PV at 0400 and 0800 UTC 26 October. These two times are representative of the entire 12-h period and demonstrate that the U_{pert} PV maximum was located just east of a region of significant negative PV advection. Importantly, however, the positive PV advection region just east of the U_{pert} PV maximum was weaker in magnitude and displaced farther from the U_{pert} PV maximum itself. As a result of this circumstance, a persistent, progressive erosion of the U_{pert} PV feature was accomplished by horizontal PV advection in the 12-h period from 0000 to 1200 UTC 26 October. It is im-

⁴ Calculations of the wavelength of the U_{pert} PV anomaly suggest a decrease of nearly 20% during this same 24-h interval. Since penetration depth varies linearly with wavelength, we estimate that approximately one-third of the observed decrease in penetration depth resulted from a reduction in the amplitude of the U_{pert} PV anomaly.

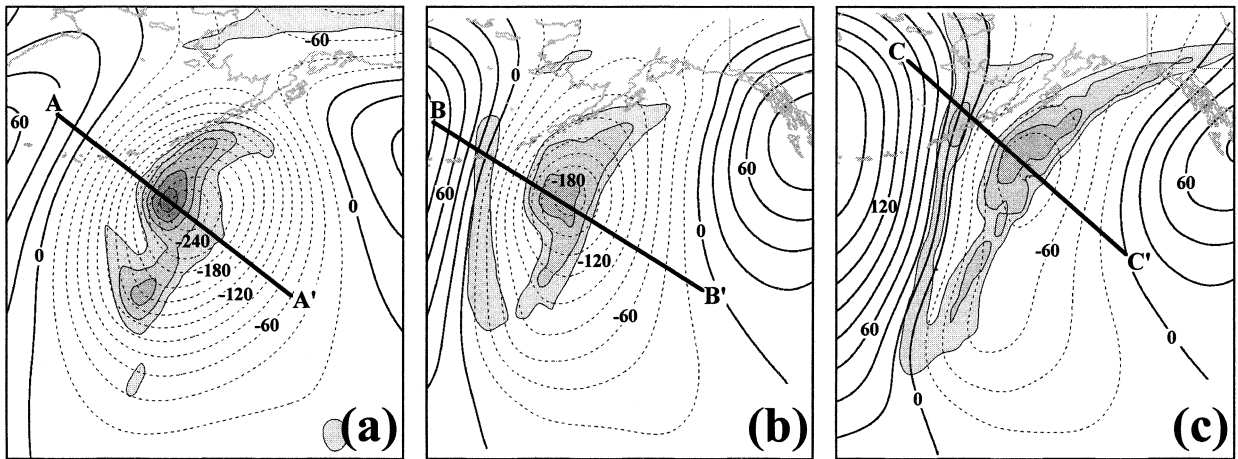


FIG. 13. (a) As for Fig. 9a but with 300–250-hPa column-averaged perturbation PV at 0000 UTC 26 Oct superimposed. Vertical cross section along line A–A' is shown in Fig. 14a. (b) As for Fig. 9b but with 300–250-hPa column-averaged perturbation PV at 1200 UTC 26 Oct superimposed. Vertical cross section along line B–B' is shown in Fig. 14b. (c) As for Fig. 9c but with 300–250-hPa column-averaged perturbation PV at 0000 UTC 27 Oct superimposed. Vertical cross section along line C–C' is shown in Fig. 14c.

portant to note that the PV advection was not entirely responsible for the observed decrease in $U_{\text{pert}} \text{ PV}$ —though it was the most significant factor in that decrease. Other nonconservative processes such as turbulence and

diabatic effects other than LHR likely also contributed to the decrease in $U_{\text{pert}} \text{ PV}$, though such were not accounted for in this analysis. The primacy of negative horizontal PV advection in eroding the $U_{\text{pert}} \text{ PV}$ in this

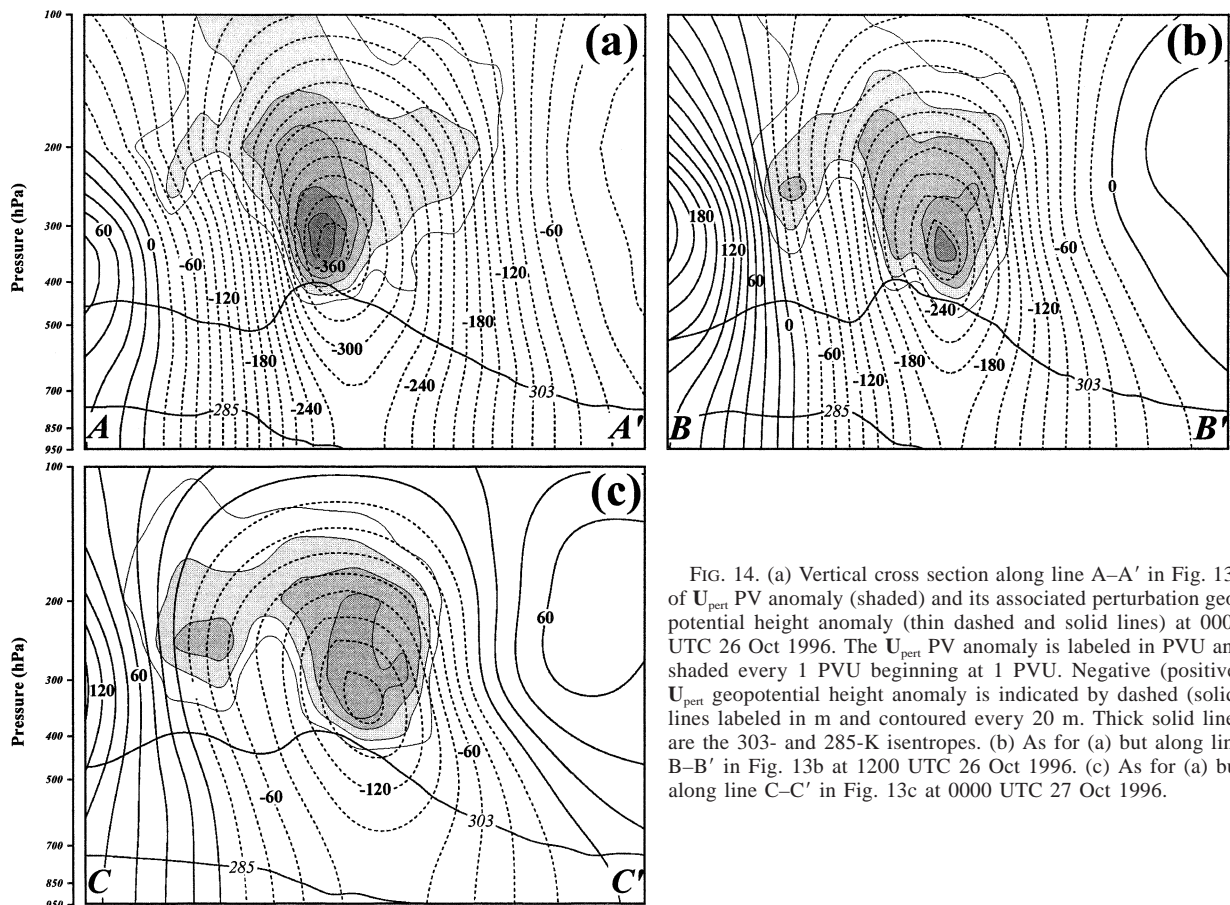


FIG. 14. (a) Vertical cross section along line A–A' in Fig. 13a of $U_{\text{pert}} \text{ PV}$ anomaly (shaded) and its associated perturbation geopotential height anomaly (thin dashed and solid lines) at 0000 UTC 26 Oct 1996. The $U_{\text{pert}} \text{ PV}$ anomaly is labeled in PVU and shaded every 1 PVU beginning at 1 PVU. Negative (positive) $U_{\text{pert}} \text{ geopotential height anomaly}$ is indicated by dashed (solid) lines labeled in m and contoured every 20 m. Thick solid lines are the 303- and 285-K isentropes. (b) As for (a) but along line B–B' in Fig. 13b at 1200 UTC 26 Oct 1996. (c) As for (a) but along line C–C' in Fig. 13c at 0000 UTC 27 Oct 1996.

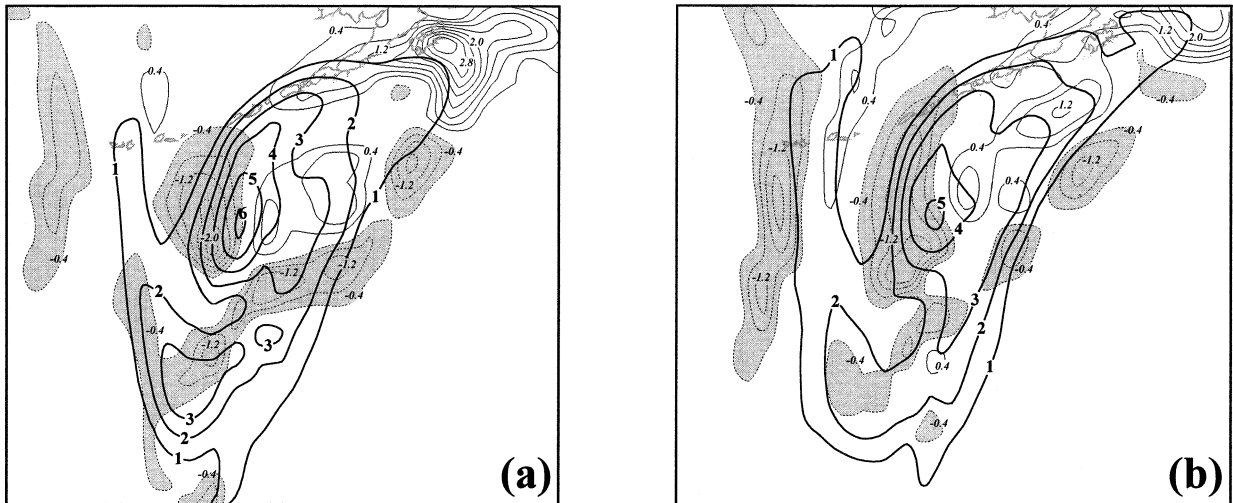


FIG. 15. (a) The 300–250-hPa column-averaged perturbation PV (thick lines) and 300–250-hPa column-averaged PV advection (thin dashed and solid lines) at 0400 UTC 26 Oct 1996. Perturbation PV is labeled in PVU and contoured every 1 PVU beginning at 1 PVU. Negative PV advection is indicated by dashed lines labeled in PVU day⁻¹ and contoured and shaded every -0.4 PVU day⁻¹ beginning at -0.4 PVU day⁻¹. Positive PV advection is indicated by solid lines labeled in PVU day⁻¹ and contoured every 0.4 PVU day⁻¹ beginning at 0.4 PVU day⁻¹. (b) As for (a) but for 0800 UTC 26 Oct 1996.

12-h period, and thus in promoting surface cyclolysis, represents an example of clear overlap between the PV and traditional diagnostic perspectives on cyclone intensification as the latter emphasizes the effect of vorticity advection on development.

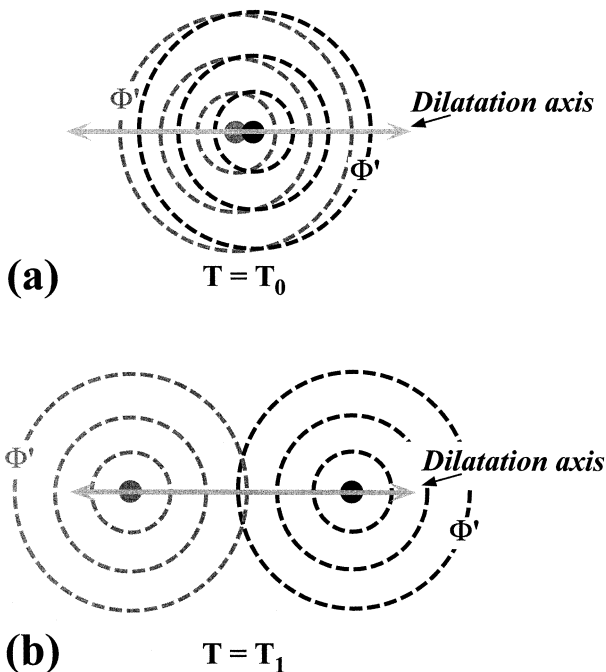


FIG. 16. Schematic illustrating the role of deformation in PV attenuation. (a) Initial juxtaposition of two like-signed PV anomalies with associated geopotential height perturbations. Gray double-shafted arrow represents axis of dilatation of the environmental deformation. (b) Subsequent positions of the two PV anomalies after prolonged exposure to the environmental deformation.

As noted earlier, the reduction in magnitude of the U_{pert} PV anomaly was not particularly impressive in the 12-h period from 1200 UTC 26 October to 0000 UTC 27 October. Nonetheless, an equivalent weakening of its associated lower-tropospheric circulation occurred in this interval. This weakening is likely attributable to the morphological evolution of the PV anomaly during these 12 h. As shown in Fig. 13, a significant thinning and elongating of the U_{pert} PV anomaly occurred between 1200 UTC 26 October and 0000 UTC 27 October. We shall hereafter refer to this thinning and elongating of the perturbation PV as “attenuation” of the PV.

Prior studies of cyclone life cycles have emphasized the role of environmental deformation in promoting an increased isotropy in the perturbation PV field (Nielsen-Gammon and Lefevre 1996; Hakim et al. 1996; Morgan and Nielsen-Gammon 1998; Lackmann et al. 1999). The so-called superposition principle (Morgan and Nielsen-Gammon 1998) describes the intensification of the perturbation heights associated with a PV anomaly when that anomaly is made more isotropic. The deformation can just as well promote an increased anisotropy in the perturbation PV. What we have termed attenuation is the opposite of superposition; the tendency for weakening of the perturbation heights associated with a PV anomaly when that anomaly is made more anisotropic. The attenuation principle is illustrated in schematic form in Fig. 16. When two like-signed PV anomalies, each with an associated geopotential height perturbation, are in close proximity to one another, their discrete perturbation heights sum to a larger total perturbation height (Fig. 16a). If deformation in the flow promotes a separation of these PV anomalies, the sum of the height perturbation is decreased (Fig. 16b). In such a case, one could say that the PV anomaly has been attenuated.

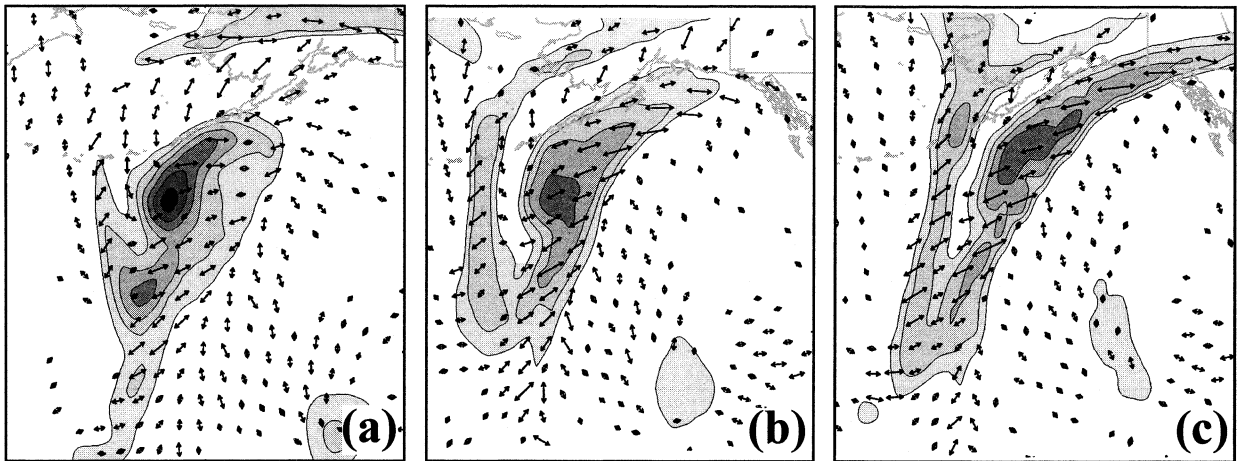


FIG. 17. (a) The 300–250-hPa column-averaged perturbation PV (shaded) and axes of dilatation (double-shafted arrows) of the 300-hPa flow at 0000 UTC 26 Oct 1996; PV is labeled in PVU and shaded every 1 PVU beginning at 1 PVU. Length of the arrows indicates the magnitude of the resultant deformation. (b) As for (a) but for 1200 UTC 26 Oct 1996. (c) As for (a) but for 0000 UTC 27 Oct 1996.

An analysis of the 300–250-hPa column-average perturbation PV along with the axes of dilatation of the 300-hPa flow is shown in Fig. 17. Beginning at 1200 UTC 26 October (Fig. 17b), the axes of dilatation of the flow were roughly parallel to the long axis of the U_{pert} PV anomaly. Thus, the deformation forced the attenuation of the perturbation PV feature. By 0000 UTC 27 October, the axes of dilatation continued to be aligned nearly along the axis of the perturbation PV (Fig. 17c) while the magnitude of the deformation had increased. Even more rapid attenuation of the perturbation PV feature resulted with an attendant weakening of the geopotential height perturbation in the lower troposphere. This analysis suggests that a rapid stretching of the upper-tropospheric perturbation PV feature was yet another underlying physical factor in the rapid surface cyclolysis observed in this case.

5. Discussion

In the present study a piecewise inversion of the full Ertel PV has been employed to gain insight into the processes that conspired to produce the rapid surface cyclolysis observed south of the Aleutian Islands on 26–27 October 1996. It was found that the geopotential height perturbations associated with the upper-level (U_{pert}) PV anomaly exerted the greatest control on the surface cyclolysis. In the 12-h period from 0000 to 1200 UTC 26 October the U_{pert} anomaly was reduced in magnitude through negative PV advection near the tropopause. The corresponding increase in the associated height perturbation was felt throughout the domain and accounted for the majority of the lower-tropospheric height rises characterizing the cyclolysis in that period. In the subsequent 12-h period of rapid cyclolysis, the U_{pert} PV anomaly was stretched by the deformation field associated with a southwesterly jet streak. This stretching, an example of what we refer to as attenuation,

rendered the U_{pert} PV anomaly more anisotropic and reduced the geopotential height anomaly associated with it at every level in the atmosphere.

In the present case, the influence of PV advection on the transformation of the tropopause PV structure provides a clear conceptual link between the PV diagnostic view and what might be termed the basic-state variable view of surface development. In the latter, lower-tropospheric development is directly related to differential vorticity advection [i.e., thermal wind advection of geostrophic vorticity as in Sutcliffe (1947) and Trenberth (1978)]. From the piecewise PV inversion perspective the closely related Ertel PV advection is the critical factor in the diagnosis of development. This very connection, explored within a QG framework, lies at the heart of the powerful piecewise tendency diagnostic (PTD) method developed by Nielsen-Gammon and Leffevre (1996). A distinct advantage of the PV approach to assessing development is that a more precise quantification of the effects of (potential) vorticity advection forcing on lower-tropospheric disturbances is possible. In addition, the higher-order balance condition employed in the Ertel PV perspective ensures a more comprehensive diagnostic result.

The upper-tropospheric evolution of the present case resembles that of the LC1 life cycle described by Thorncroft et al. (1993). They showed that large-scale, anticyclonic, barotropic shear promotes anticyclonic wave-breaking during which a positively tilted tropopause PV feature undergoes progressive thinning and elongation. The attenuation of the U_{pert} PV anomaly between 1200 UTC 26 October and 0000 UTC 27 October was forced by tropopause-level deformation as shown in Fig. 17. The requisite deformation was provided by the jet streak located on the downstream side of the upper-level trough associated with the object cyclone. The composition of this deformation field at a representative time (0000

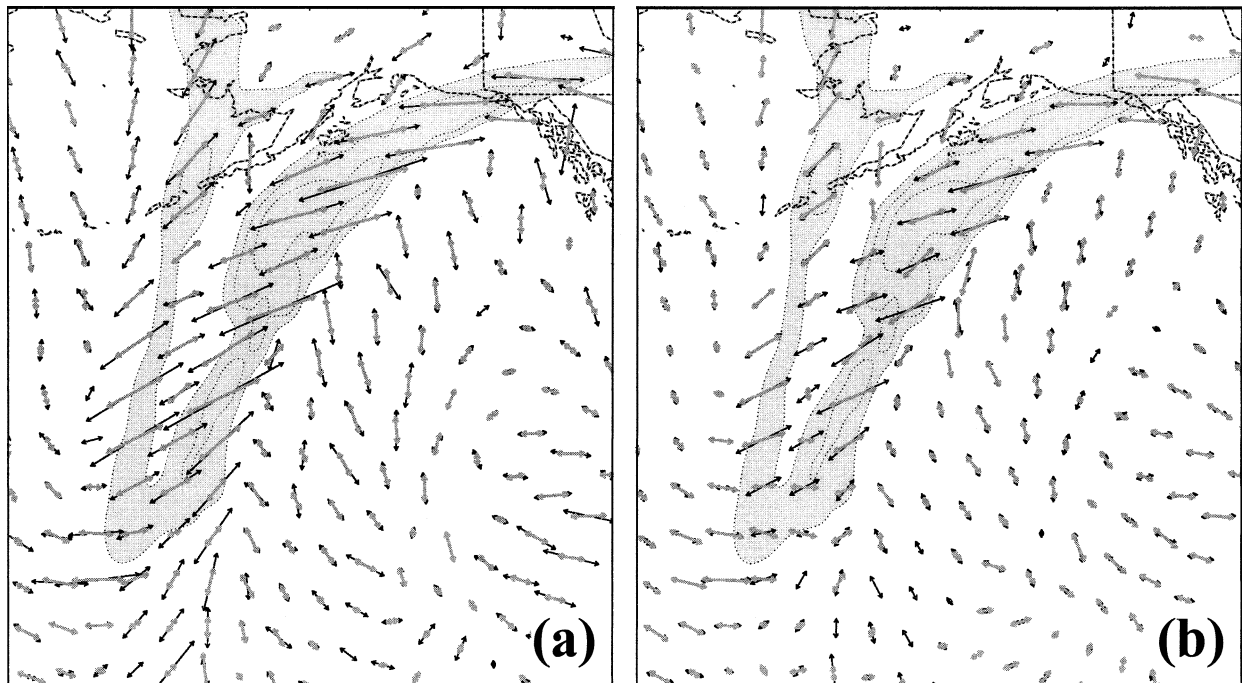


FIG. 18. (a) Axes of dilatation of the full wind (black double-shafted arrows) and the total balanced flow (thick gray double shafted arrows) at 300 hPa for 0000 UTC 27 Oct 1996. (b) Axes of dilatation of the total balanced flow (black double-shafted arrows) and the U_{pert} flow (thick gray double shafted arrows) at 300 hPa for 0000 UTC 27 Oct 1996.

UTC 27 October) is illustrated in Fig. 18. The total balanced flow contributes a sizeable portion of the total deformation in the region of interest near the U_{pert} PV anomaly (Fig. 18a). It is clear from Fig. 18a that a respectable portion of the total deformation is related to the unbalanced portion of the flow (as defined by Davis et al. 1996), which is often large in association with wind speed maxima. Figure 18b demonstrates that the largest portion of the balanced flow deformation is associated with the U_{pert} PV anomaly itself. Neither the mean flow (as defined for our inversion diagnostics) nor the M_{pert} flow at tropopause level contributes significantly to the deformation in the region of interest. It appears, therefore, that flow associated with the perturbations, and not the large-scale background flow, plays the most prominent role in the attenuation process in this case. Whether or not this is generally the case for LC1-type evolutions is a question for future research.

In addition to the aforementioned tropopause-level effects, the cyclone life cycle is also characterized by structural evolution that effects the lower-tropospheric frontal structure and temperature distribution. Analysis of the October 1996 storm indicates that the lower-tropospheric thermal anomaly, S_{pert} , can play a discernible role in surface cyclolysis. In the present case the S_{pert} anomaly raced away from the 950-hPa geopotential minimum after 1200 UTC October 26, bringing with it its associated 950-hPa geopotential height anomaly. We suggest that this behavior is related synoptically to the process of occlusion wherein the geopotential height

minimum becomes progressively further removed from the peak of the original warm sector. Such a process can, under certain circumstances, be accelerated by the effects of latent heat release as suggested by Davis (1992). In that work, piecewise PV diagnosis was employed to examine the influence of latent heat release on the life cycles of two different cyclones. In one (the December case), it was inferred that the low-level diabatically generated PV anomaly (M_{pert}) increased the eastward propagation of the surface thermal anomaly (S_{pert}). Examination of the M_{pert} winds and full PV at 950 hPa from the present case (not shown) suggests that the M_{pert} winds acted to advect the 950-hPa PV eastward, thus contributing to the removal of the 950-hPa S_{pert} geopotential height perturbation minimum from the vicinity of the surface low. In this way, latent heat release directly influenced the propagation of the lower-tropospheric thermal anomaly in a manner that promoted surface cyclolysis.

Another likely footprint of latent heat release on the evolution of this rapidly decaying cyclone is evident in the upper-tropospheric PV structure itself (shown in Fig. 7). The axis of PV minimum north of the Aleutian Islands in Fig. 7a is coincident with the portion of the cloud shield located in the occluded quadrant of the cyclone. The presence of cloudiness there is suggestive of middle-tropospheric latent heat release in that region. It is likely that diabatic redistribution of PV associated with the latent heat release was a primary factor in the creation of this tropopause PV minimum. The sizeable

PV gradient on the southeast edge of the PV minimum provided a necessary ingredient for the subsequent large negative PV advections to the southeast that served to erode the U_{pert} PV anomaly through 1200 UTC 26 October. Thus, despite the fact that the lower-tropospheric M_{pert} geopotential height anomalies were not a significant contributor to the cyclolysis, it appears likely that the effects of latent heat release, integrated over the full cyclone life cycle, did play some role in this case of cyclolysis. Preliminary examination of a companion adiabatic simulation of the decay phase of the present case (1200 UTC 25 October–1200 UTC 27 October) suggests that the rapidity of decay is only modestly effected by inclusion of latent heat release in that 48-h period. As suggested above, however, it is the effects of latent heat release integrated over the full life cycle that are likely more relevant to determining the role of latent heat release in cyclolysis. Such investigations are left to future work involving examination of other cases.

The piecewise PV inversion diagnosis of this rapid cyclolysis event does not explicitly take boundary layer friction into account. Despite this fact, the rapidity of cyclolysis is well described in the analysis. In fact, the increases in the 950-hPa geopotential height anomalies faithfully capture the observed height rises. Since these geopotential height anomalies are directly related to their respective PV anomalies by an inversion operator that makes no reference to lower-tropospheric friction, this fidelity suggests that boundary layer friction is not a major contributor to rapid surface cyclolysis. This suggestion is consistent with similar inferences made based upon the synoptic climatology of rapid cyclolysis events presented in Martin et al. (2001). In addition, a comparison simulation run without boundary layer friction (not shown) filled 29 hPa over the 36-h period of most rapid cyclolysis. We therefore conclude that boundary layer friction, though certainly a contributing factor to surface cyclolysis in general, is not a first-order forcing for particularly rapid surface cyclolysis. Stated alternatively, rapid surface cyclolysis is unlikely to occur except in a large-scale environment that promotes the rapid erosion of upper-tropospheric PV anomalies associated with synoptic-scale short waves.

6. Conclusions

From 1800 UTC 25 October to 0600 UTC 27 October 1996 a surface cyclone south of the Aleutian Islands experienced a minimum sea level pressure rise of 35 hPa. This rapid surface cyclolysis was associated with a rapid transformation of the upper-tropospheric structure associated with the storm. The method of piecewise potential vorticity inversion (Davis and Emanuel 1991) was employed, using output from a successful numerical simulation of the event, to diagnose this rapid decay. It was found that the observed height rises characterizing the rapid decay were largely the result of 950-hPa perturbation geopotential height changes (at the position of

the low-level cyclone) associated with the upper-level PV anomaly (U_{pert}). In the 12-h period from 0000 to 1200 UTC 26 October, a significant reduction in the magnitude of the U_{pert} PV anomaly was accomplished primarily by the action of upper-tropospheric, negative PV advection by the full wind. Coincident with the erosion of the PV anomaly aloft, the associated 950-hPa geopotential height anomaly increased. In the subsequent 12-h period of decay, the U_{pert} PV anomaly was attenuated (i.e., made more anisotropic) by the deformation field associated with a jet streak on the downstream side of the associated upper-level trough. The majority of this deformation was provided by balanced flow associated with the perturbations, most notably the U_{pert} PV anomaly. The 950-hPa perturbation geopotential height associated with the attenuated U_{pert} PV anomaly correspondingly weakened, resulting in additional height rises.

The 950-hPa geopotential height changes associated with the lower-level PV anomaly (S_{pert}) were found to exert a usually modest (sometimes significant) influence on lower-tropospheric height rises. Meanwhile the 950-hPa geopotential height changes associated with the diabatically produced midtropospheric PV anomaly (M_{pert}) were negligible. It is important to note that consideration of the M_{pert} height changes is only one way to gauge the role of latent heat release on this cyclolysis event. The circulation associated with the M_{pert} PV anomaly apparently acted to accelerate the S_{pert} anomaly to the east thereby contributing to the decay. Additionally, the diabatic redistribution of PV associated with diabatic heating may well have indirectly contributed to the negative upper-tropospheric PV advection found to be responsible for eroding the U_{pert} PV anomaly from 0000 to 1200 UTC 26 October. Despite the existence of these alternative modes of influence, a companion adiabatic numerical simulation (not shown) revealed little difference in the overall evolution of the storm during the decay phase as compared to the object run. Thus, it appears that decay phase latent heat release played a minor role in the rapid cyclolysis described here. Our preliminary analysis of another rapid cyclolysis event suggests that this may not always be the case. Additionally, it is suggested that only by examining the effect of latent heat release integrated over the entire cyclone life cycle can its true role in cyclolysis be discerned.

Finally, it appears that boundary layer friction was not a major contributing factor to the rapid surface cyclolysis observed in this case. Evidence for this assertion arises from the fact that the PV inversion procedure, which makes no reference to surface friction, nonetheless produces a faithful depiction of the height rises in the lower troposphere. Additional support for this assertion comes from the fact that a companion simulation, run without boundary layer friction, exhibited nearly the same filling rate as the object simulation. Thus, we conclude that rapid surface cyclolysis is predominantly a function of large-scale environments that promote rap-

id erosion of the upper-tropospheric PV anomalies associated with synoptic-scale short waves.

Acknowledgments. This research was supported by the National Science Foundation under Grant ATM-9733127. The thoughtful comments and suggestions of two anonymous reviewers are greatly appreciated.

REFERENCES

- Bretherton, F. P., 1966: Baroclinic instability and the shortwave cutoff in terms of potential vorticity. *Quart. J. Roy. Meteor. Soc.*, **92**, 335–345.
- Cammas, J.-P., D. Keyser, G. M. Lackmann, and J. Molinari, 1994: Diabatic redistribution of potential vorticity accompanying the development of an outflow jet within a strong extratropical cyclone. Preprints, *Int. Symp. on the Life Cycles of Extratropical Cyclones*, Vol. II, Bergen, Norway, Geophysical Institute, University of Bergen, 403–409.
- Charney, J., 1955: The use of the primitive and balance equations. *Tellus*, **7**, 22–26.
- Davis, C. A., 1992: A potential vorticity diagnosis of the importance of initial structure and condensational heating in observed cyclogenesis. *Mon. Wea. Rev.*, **120**, 2409–2428.
- , and K. A. Emanuel, 1991: Potential vorticity diagnostics of cyclogenesis. *Mon. Wea. Rev.*, **119**, 1929–1953.
- , E. D. Grell, and M. A. Shapiro, 1996: The balanced dynamical nature of a rapidly intensifying oceanic cyclone. *Mon. Wea. Rev.*, **124**, 3–26.
- Dudhia, J., 1996: A multi-layer soil temperature model for MM5. Preprints, *Sixth PSU/NCAR Mesoscale Model User's Workshop*, Boulder, CO, NCAR, 49–50.
- Emanuel, K. A., M. Fantini, and A. J. Thorpe, 1987: Baroclinic instability in an environment of small stability to slantwise convection. Part I: Two-dimensional models. *J. Atmos. Sci.*, **44**, 1559–1573.
- Ertel, H., 1942: Ein neuer hydrodynamischer Wirbelsatz. *Meteor. Z.*, **59**, 271–281.
- Grell, G. A., 1993: Prognostic evaluation of assumptions used by cumulus parameterizations. *Mon. Wea. Rev.*, **121**, 764–787.
- , J. Dudhia, and D. R. Stauffer, 1994: A description of the fifth-generation Penn State/NCAR Mesoscale Model (MM5). NCAR Tech. Note NCAR/TN-398+STR, 117 pp.
- Hakim, G. J., D. Keyser, and L. F. Bosart, 1996: Diagnosis of tropopause-based coherent structures. Preprints, *Seventh Conf. on Mesoscale Processes*, Reading, United Kingdom, Amer. Meteor. Soc., 17–22.
- Hong, S.-Y., and H.-L. Pan, 1996: Nonlocal boundary layer vertical diffusion in a medium-range forecast model. *Mon. Wea. Rev.*, **124**, 2322–2339.
- Hoskins, B. J., M. E. McIntyre, and A. W. Robertson, 1985: On the use and significance of isentropic potential vorticity maps. *Quart. J. Roy. Meteor. Soc.*, **111**, 877–946.
- Korner, S. O., and J. E. Martin, 2000: Piecewise frontogenesis from a potential vorticity perspective: Methodology and a case study. *Mon. Wea. Rev.*, **128**, 1266–1288.
- Lackmann, G. M., D. Keyser, and L. F. Bosart, 1999: Energetics of an intensifying jet streak during the Experiment on Rapidly Intensifying Cyclones over the Atlantic (ERICA). *Mon. Wea. Rev.*, **127**, 2777–2795.
- Martin, J. E., R. D. Grauman, and N. Marsili, 2001: Surface cyclolysis in the North Pacific Ocean. Part I: A synoptic climatology. *Mon. Wea. Rev.*, **129**, 748–765.
- Morgan, M. C., and J. Nielsen-Gammon, 1998: Using tropopause maps to diagnose midlatitude weather systems. *Mon. Wea. Rev.*, **126**, 2555–2579.
- Nielsen-Gammon, J., and R. Lefevre, 1996: Piecewise tendency diagnosis of dynamical processes governing the development of an upper-tropospheric mobile trough. *J. Atmos. Sci.*, **53**, 3120–3142.
- Raymond, D. J., 1992: Nonlinear balance and potential vorticity thinking at large Rossby number. *Quart. J. Roy. Meteor. Soc.*, **118**, 987–1015.
- Rossby, C. G., 1940: Planetary flow patterns in the atmosphere. *Quart. J. Roy. Meteor. Soc.*, **66**, 68–87.
- Sinclair, M. R., 1997: Objective identification of cyclones and their circulation intensity, and climatology. *Wea. Forecasting*, **12**, 595–612.
- Sutcliffe, R. C., 1947: A contribution to the problem of development. *Quart. J. Roy. Meteor. Soc.*, **73**, 370–383.
- Thorncroft, C. D., B. J. Hoskins, and M. E. McIntyre, 1993: Two paradigms of baroclinic-wave life-cycle behaviour. *Quart. J. Roy. Meteor. Soc.*, **119**, 17–55.
- Trenberth, K. E., 1978: On the interpretation of the diagnostic quasi-geostrophic omega equation. *Mon. Wea. Rev.*, **106**, 131–137.